



# Eccentricity dependent changes of density, spacing and packing arrangement of parafoveal cones

Marco Lombardo<sup>1</sup>, Sebastiano Serrao<sup>1</sup>, Pietro Ducoli<sup>1</sup> and Giuseppe Lombardo<sup>2,3</sup>

<sup>1</sup>Fondazione G.B. Bietti IRCCS, Rome, Italy, <sup>2</sup>CNR-IPCF Unit of Support Cosenza, University of Calabria, Rende, Italy, and <sup>3</sup>Vision Engineering, Rome, Italy

**Citation information:** Lombardo M, Serrao S, Ducoli P & Lombardo G. Eccentricity dependent changes of density, spacing and packing arrangement of parafoveal cones. *Ophthalmic Physiol Opt* 2013. doi: 10.1111/opo.12053

**Keywords:** adaptive optics, cone density, cone spacing, cone packing arrangement

*Correspondence:* Marco Lombardo  
E-mail address: mlombardo@visioeng.it

Received: 22 October 2012; Accepted: 1 March 2013

## Abstract

*Purpose:* To investigate the distribution of cone density and spacing as well as the preferred packing arrangement of the cone mosaic as a function of retinal eccentricity.

*Methods:* An adaptive optics retinal camera (*rtx1*, [www.imagine-eyes.com](http://www.imagine-eyes.com)) was used to obtain images of the parafoveal cone mosaic in nineteen healthy volunteers. Cone density and spacing were estimated for each subject (both eyes) using a sampling window of 80 × 80 pixels, at 250-, 450-, 650- and 1100- $\mu\text{m}$  eccentricities from the fovea along the nasal and temporal retina of both eyes. The inter-subject and intra-subject variation of cone density and spacing were calculated via Coefficient of Variation (CoV). Cone packing arrangement was assessed using Voronoi analysis; calculations were done over 1024 × 128 pixels image sections of the cone mosaic across the horizontal meridian from 200- to 1050- $\mu\text{m}$  eccentricities.

*Results:* The inter-subject variation of parafoveal cone density ranged between 10% and 15% ( $p < 0.001$ ) and the intra-subject variation of cone density was lower than 8% in all subjects, except for two. The cone spacing values showed a moderate inter-subject (CoV < 7%;  $p < 0.001$ ) and a low intra-subject variation (CoV < 4% in all subjects, except for two cases). In the parafoveal region, 40–50% of cones were hexagonally arranged; the percentage of non-hexagonal Voronoi tiles increased at greater eccentricities.

*Conclusion:* The use of multiple and complementary metric descriptors allows for a more detailed description of packing distribution and preferred arrangement of cone photoreceptors across the parafoveal retina.

## Introduction

Even though adaptive optics (AO) retinal imaging is an established research tool, work is still needed to achieve a widespread clinical use.<sup>1,2</sup> A current limit of AO imaging is the time required to obtain, process and analyse the retinal images: the continuous advances in the development of automated and reliable methods to evaluate the retinal micro-structures, which include the photoreceptors, vessels and nerve fibre bundles,<sup>3–7</sup> are going to resolve this matter. Accurate automated routines and reliable metric descriptors are indeed mandatory when large quantities of data are

needed to be analysed before AO retinal imaging could be considered to be a practical tool in a clinical setting.

Among previous studies that evaluated the cone mosaic structure, the most frequently adopted approach involved counting the number of cones.<sup>8–13</sup> Cone density was in general calculated by dividing the number of cones recorded by the sampling retinal area. Since cones show a higher intensity than other parts of the retinal image (i.e., the cone behaves as a waveguide and its centre is normally brightest), one can identify them based on this characteristic: the method is therefore effective for images where cones present themselves as local intensity maxima. Images may

still display variations in brightness and contrast due to anisotropies in underlying and overlying tissue layers despite the fact that the photoreceptor mosaic is well preserved.<sup>14–16</sup> It often occurs that some of the cones cannot be adequately labelled, leading to *undersampling* errors. Estimation errors of automated cone labelling were found to range between 0% and 9% in the parafoveal retina.<sup>17,18</sup> However, manual checking of the algorithm performance has been shown to minimise the error of estimates.<sup>17</sup>

Recent studies are demonstrating that the estimation of cone density alone appears not to represent an adequate method to evaluate the health and integrity of the cone mosaic and more importantly assess pathologic cone losses at an early stage of retinal diseases.<sup>19,20</sup> There are several known limits of cone density measurements,<sup>10,11,13,17,21,22</sup> which include: (1) the lack of a standardised method, (2) missing a cone leading to cone density undersampling dependent on window area and eccentricity, (3) instabilities in fixation and changes in cone density, primarily toward the fovea, limiting the ability to compare cone density even in the same eye longitudinally over time and (4) inter-subject variations of cone density as cone density has been shown to vary between 12% and 20% within 2 mm eccentricity in healthy adults.

The use of only the cone density method to describe the cone mosaic structure could potentially miss the opportunity for applying AO imaging to the detection of a progressive retinal disease in advance. An additional approach useful for describing the cone photoreceptor mosaic consists of examining the spatial distribution of cones.<sup>22–30</sup> Assessment of the spacing and the packing arrangement of the cones in combination with cone density could provide a more comprehensive picture of the cone mosaic integrity than estimating cone density alone. This approach could also potentially minimise the error estimates when comparing values between eyes with presumptive retinal diseases and controls in clinical studies.

The scope of the present work was to use multiple cone metrics for the statistical description of the parafoveal cone mosaic: the cone density and spacing distribution as well as the preferred cone packing arrangement were evaluated as a function of retinal eccentricity in a healthy adult population.

## Materials and methods

Healthy adult subjects were recruited. The inclusion criteria were as follows: Optimal visual acuity better than 1.0 logMAR (Snellen 6/6 or 20/20), no history or any sign of systemic or eye diseases, no previous eye surgery and astigmatism less than 2.50 dioptres. The protocol was approved by the local Ethical Committee and the study adhered to the tenets of Declaration of Helsinki. All the subjects gave

written informed consent after a full explanation of the procedure.

Each subject received a complete eye examination, which included a subjective refraction, non-contact ocular biometry via partial coherence interferometry (IOL Master, [www.iolmaster-online.zeiss.com/](http://www.iolmaster-online.zeiss.com/)) and retinal imaging using a *Spectralis* (SLO/SD-OCT, [www.heidelbergengineering.com](http://www.heidelbergengineering.com)). A flood-illuminated AO retinal camera (*rtx1*, [www.imagine-eyes.com](http://www.imagine-eyes.com))<sup>4,13</sup> was used to evaluate the parafoveal cone mosaic. The apparatus' core components include a wavefront sensor (HASO 32-eye, [www.imagine-eyes.com](http://www.imagine-eyes.com)), a correcting element (Mirao 52-e, [www.imagine-eyes.com](http://www.imagine-eyes.com)) and a CCD camera ([www.roperscientific.com](http://www.roperscientific.com)). One of the devices' source (low-coherence SLD, centred at 750 nm) is used by the AO instrument to measure and correct optical aberrations and, at the same time, to control the focus at retinal layers. The second source (a light emitting diode, with wavelength centred at 850 nm) provides uniform illumination across the retinal area to be imaged subtending 4 degrees of visual angle. The theoretical lateral optical resolution of the instrument is 2  $\mu\text{m}$ . The pixel to retina ratio of the raw single image frame is 1:1.6  $\mu\text{m}$ .

## AO retinal imaging

The AO imaging sessions were conducted after dilating the pupils with one drop of 1% tropicamide. During AO imaging, fixation was maintained having the patient fixate the internal target of the instrument moved by the investigator at fixed retinal locations. In this study, each subject was instructed to fixate at 0°, 1°, 2°, 4° and 6° eccentricity along the nasal and temporal retina; a video camera monitored the subjects' pupil and eye movements. At each eccentricity, a sequence of 40 frames (9.5 frames per second) was acquired in both eyes of each subject.

A proprietary programme provided by the manufacturer has been used to correct for distortions within frames of the raw image sequence and to correlate and frame-average in order to produce a final image with enhanced signal-to-noise ratio. Furthermore, processing of the final image included cubic interpolation in order to increase the pixel to retina ratio to 1:0.8  $\mu\text{m}$  (here used for retinal distance calculation). Frames exhibiting large motion artefacts due to eye movement or blinking were manually removed before processing. For each eye, more than 30 frames were used at each eccentricity location.

Before analysis, each image was converted from degrees of visual angle to micrometres on the retina: for this purpose, we used the nonlinear formula of Drasdo and Fowler<sup>13,31,32</sup> and the Gullstrand schematic model eye parameterised by the biometry measurements from each eye obtained with the IOL Master. The spectacle corrected magnification factor ( $\text{RMF}_{\text{corr}}$ ) was calculated in order to

correct for the differences in optical magnification and thus retinal image size between eyes. The  $RMF_{corr}$  was estimated for each eye by consideration of the axial length and the trial lens added to the system to compensate for defocus.<sup>11,13</sup> The spectacle vertex distance was set at 14 mm for all eyes.

### AO retinal image analysis

The Image cone labelling process was performed using an algorithm implemented with the image processing toolbox in Matlab (www.mathworks.com), as previously described by Li and Roorda<sup>8</sup> with enhancements that have accumulated over time. Filtering and morphological image processing were applied to isolate the higher intensity signals corresponding to presumably cone photoreceptors. Filtering parameters were manually selected based on the estimated minimum diameter of two adjacent cones in order to avoid potential mistakes by eliminating locations that were too close together to be cones. An empirically determined intensity threshold (0.18) was applied on the set of identified local maxima to further reduce false positive. A different value of the filtering parameter, from 10 to 20 pixels, was used at each eccentricity location.

Images of adjacent areas of the retina along the horizontal meridian were assembled together after processing to create a montage that covered up to  $6^\circ$  eccentricity from the foveal centre reference point. Cone density (cones/mm<sup>2</sup>) was measured at 250-, 450-, 650- and 1100- $\mu$ m eccentricities from the foveal centre reference point along the nasal and temporal retina. Eccentricity was computed as the distance between the centre of each window and the foveal centre reference point (identified as the point with fixation coordinates:  $x = 0^\circ$ ,  $y = 0^\circ$ ).<sup>4,13</sup> Sampling windows were intentionally taken in areas devoid of large blood vessels. The cone density for a given retinal eccentricity was composed by the data values (repeated twice) among a  $80 \times 80$  pixels window. The cone density was verified by three investigators (ML, SS and GL) in order to minimise the possible error in cone identification of the automated software. Errors included oversampling (e.g., rods, cones that were misidentified) and/or under-sampling (e.g., cones not identified).

The  $x$ - $y$  coordinates of the labelled cones were stored and the centre-to-centre cone distances (ICD, 'cone spacing', micrometres) were calculated from them under assumption that they were hexagonally arranged.<sup>33</sup> Under this assumption, the cone spacing is determined from density counts by the following:  $ICD = 1000 \left[ \frac{2}{\sqrt{3D}} \right]^{1/2}$ , where  $D$  is the number of cones per square millimetre. Cone packing arrangement was analysed graphically using Voronoi diagrams.<sup>8,30</sup> The Voronoi tessellation was implemented by the *voronoin*

Matlab function from the bidimensional coordinates of labelled cones. Each Voronoi cell was coded by a different colour corresponding to the number of their neighbouring cones: grey = tetragonal ( $4n$ ) arrangement, yellow = pentagonal ( $5n$ ) arrangement, green = hexagonal ( $6n$ ) arrangement; blue = heptagonal ( $7n$ ) arrangement and white = octagonal ( $8n$ ) arrangement. Since packing structure tends to vary as a function of retinal eccentricity, Voronoi analysis was done in sections  $1024 \times 128$  pixels wide ( $820 \times 102 \mu\text{m}$ ) along the horizontal meridian. The Voronoi regions containing pixels that extended beyond the bounds of each section were excluded from further analysis, thus creating a buffer zone to minimise the *boundary effect*.<sup>29</sup> Figure 1 illustrates the main steps in the image analysis process.

### Statistics

Retinal data were expressed as mean  $\pm$  standard deviation. Statistics were performed using the SPSS software (version 17.0; <http://www.ibm.com/software/analytics/spss/>). Statistical significant differences were set at  $p < 0.05$  for all the tests performed.

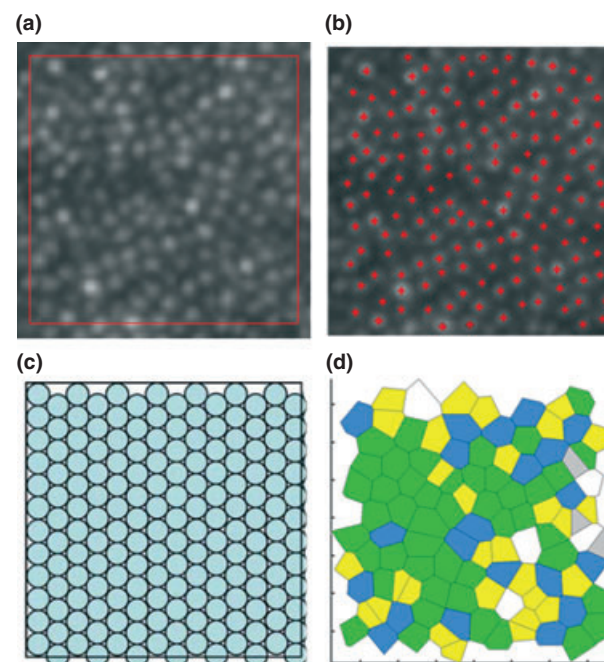


**Figure 1.** Main steps in the automated procedure used to describe the parafoveal cone mosaic structure. (a) Cone density was estimated in a  $80 \times 80$  pixels window area. (b) The cone photoreceptors labelled with the automated algorithm; cones whose centre was outside the boundary were not labelled. (c) The centre-to-centre cone spacing was calculated under the assumption that the cones were hexagonally arranged. (d) The colour-coded Voronoi domains associated with just the cone photoreceptors in the window area of panel B.

An analysis of variance was performed on cone density and spacing. The Coefficient of Variation (CoV) was used to analyse the variation of cone metrics calculated at the same retinal eccentricity along the nasal and temporal retina of fellow eyes in each subject (intra-subject variation) and in both eyes of the population study (inter-subject variation). The intraclass correlation coefficient (ICC; two-way random effects model) was calculated in order to estimate the absolute agreement between the average cone density and spacing values calculated at the various retinal eccentricities in both eyes of the population study.

The error estimates of cone density measurements, performed within two  $80 \times 80$  pixels sampling areas at the same eccentricity location by the automated algorithm, was calculated based on the intra-subject standard deviation ( $\sigma_w$ ), that is the common standard deviation of repeated measurements. To get the common  $\sigma_w$  we averaged the variances, i.e. the squares of the standard deviations, of the two repeated measures for each subject. The intra-subject standard deviation was chosen as an index of measurement error, as discussed by Bland and Altman.<sup>34,35</sup> The repeatability was defined as  $2.77\sigma_w$  and reported as percentage of the mean.

## Results

Nineteen subjects (six males and 13 females) were included in the study. The mean age was  $33.6 \pm 7.4$  years (range 24–51 years). The spherical equivalent refractive error (SEr) ranged between  $+0.25$  and  $-5.50$  D (mean:  $-1.63 \pm 2.13$  D) with astigmatism less than  $-1.25$  D when referenced to the spectacle plane. The axial length (AxL) ranged between 22.34 and 26.46 mm ( $23.99 \pm 1.13$  mm). The RMF<sub>corr</sub> ranged between 0.267 and 0.306 mm/deg ( $0.280 \pm 0.009$  mm/deg). There were no significant differ-

ences between the biometry and refractive data of the right and left eyes.

The average cone density and spacing values as a function of retinal eccentricity along the nasal and temporal retina of fellow eyes are shown in *Figure 2*. The inter-subject variation (CoV) of cone density ranged between 10% and 15% from 250- to 1100- $\mu\text{m}$  eccentricity in both eyes (F-test:  $p < 0.001$ ). The intra-subject CoV of cone density was lower than 4% in 13 of 19 subjects (68%), 16 of 19 subjects (84%) and 17 of 19 (89%) at 250-, 450- and 650- $\mu\text{m}$  eccentricity respectively. It was  $\leq 8\%$  in all subjects at 250-, 450- and 650- $\mu\text{m}$  eccentricity respectively. At 1100  $\mu\text{m}$  eccentricity, the intra-subject CoV was  $\leq 4\%$  in 13 of 19 subjects (68%) and  $\leq 8\%$  17 of 19 (89%). In two cases, a 45 years old male and a 42 years old female, the intra-subject CoV of cone density was 10% and 11% respectively.

The inter-subject variation (CoV) of ICD was 5% at 250-, 450- and 650- $\mu\text{m}$  eccentricities, increasing to 7% at 1100  $\mu\text{m}$  eccentricity in both eyes (F-test:  $p < 0.001$ ). The intra-subject variation of ICD was  $\leq 2\%$  in 16 of 19 subjects (84%) at 250- and 450- $\mu\text{m}$  eccentricity; in 18 of 19 (95%) at 650  $\mu\text{m}$  eccentricity and in 12 of 19 (63%) at 1100  $\mu\text{m}$  eccentricity. The intra-subject variation of ICD was  $\leq 4\%$  in all subjects at all eccentricities, except for two cases (the same 45 years old male and 42 years old female, as expected) at 1100  $\mu\text{m}$  eccentricity.

The highest absolute agreement ( $\text{ICC} \geq 0.828$ ;  $p < 0.001$ ) was found between values taken at equivalent eccentricity locations of the nasal and temporal retina in the same eye. A high absolute agreement ( $\text{ICC} \geq 0.706$ ;  $p < 0.001$ ) was also found between the same (i.e. nasal with nasal) and corresponding (i.e. nasal with temporal) eccentricity locations of fellow eyes. The average differences between the cone density and the ICD values of the same and corresponding eccentricity locations of fellow eyes were lower than 4% and 2%, respectively. A summary of the

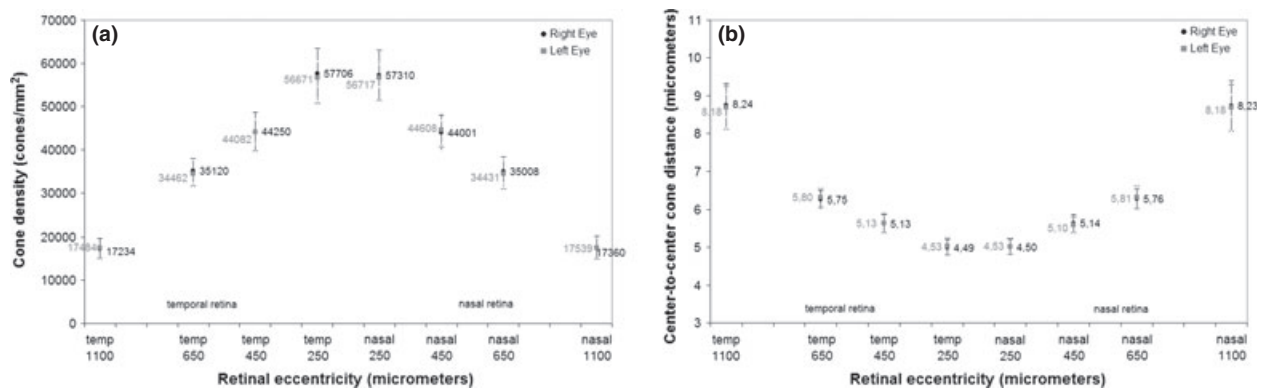


**Figure 2.** (a) The average cone density (cones/mm<sup>2</sup>) and (b) the centre-to-centre cone distance (micrometers) values, along the nasal and temporal retina of the right (black dots) and left (grey squares) eyes, are shown. The numbers show the average values at each retinal eccentricity. The vertical bars represent one S.D. from the mean.

average ICC values between the cone density and spacing values across the horizontal meridian has been uploaded as supplementary material (Table S1 and S2).

The percentage of hexagonal Voronoi regions decreased from an average  $46.1 \pm 2.6\%$  to  $37.9 \pm 2.7\%$  from 200- to 1050- $\mu\text{m}$  eccentricity. The percentage of pentagonal Voronoi regions slightly increased from an average  $25.7 \pm 1.2\%$  to  $28.0 \pm 1.0\%$ , while the percentage of heptagonal Voronoi cells was almost stable (from  $20.9 \pm 0.6\%$  to  $20.6 \pm 1.0\%$ ) across eccentricities. The percentage of Voronoi regions with  $8n$  arrangement ranged between  $4.5 \pm 1.0\%$  and  $7.2 \pm 1.4\%$  and the percentage of Voronoi with  $4n$  ranged between  $3.0 \pm 0.8\%$  and  $6.1 \pm 1.3\%$  from 200- to 1050- $\mu\text{m}$  eccentricity, respectively. At equivalent eccentricities, the average difference of the percentage of hexagonal Voronoi between the nasal and temporal regions of the same eye was  $<3\%$ ; it was lower than 7% between the same and the corresponding retinal eccentricity sections of fellow eyes in all subjects (Figure 3).

The  $\sigma_w$  of cone density was  $\leq 1800$  cones/ $\text{mm}^2$  at 250  $\mu\text{m}$  eccentricity;  $\leq 1500$  cones/ $\text{mm}^2$  at 450- and 650- $\mu\text{m}$  eccentricity;  $\leq 1000$  cones/ $\text{mm}^2$  at 1100  $\mu\text{m}$  eccentricity. This means that the difference between two measurements (repeatability of method) was lower than 6% at each eccentricity. In the case that the sampling window occurred in a retinal area with large blood vessel, the automated algorithm tended to locally misidentify cones with oversampling error (Figure 4). We discharged from analysis data acquired from windows covered  $\geq 50\%$  of their sampling area by large vessel. This occurred only in

four cases at the greatest eccentricity location (5% of all sampling windows at this eccentricity) in our series.

## Discussion

In recent years, important advances have been made to make AO retinal imaging technology a valid research tool in ophthalmology.<sup>1-7</sup> The real advantage of AO retinal imaging is to provide the clinician with micrometric lateral resolution of the retinal tissue *in vivo*, potentially allowing for earlier detection of the pathological changes of photoreceptors and other retinal structures (i.e. capillaries and nerve fibre bundles).

In a continuing effort to validate the use of AO retinal imaging for the description of the cone mosaic, research groups are showing various statistical methods, such as the estimation of cone density and cone spatial distribution.<sup>8-13,21-30</sup> It remains under scrutiny whether or not a single metric can reliably describe the cone mosaic integrity and, most of all, the pathologic disruption of the cone mosaic. In this study, we aimed to estimate and statistically describe the distribution of density, spacing and the preferred packing arrangement of the cone photoreceptors as a function of retinal eccentricity across the parafovea in a healthy population. The use of multiple and complementary metrics could be more advantageous than a single metric: a first advantage can be to provide a more comprehensive picture of the cone mosaic through the (1) definition of a threshold in the normative data for each metric, (2) definition of both the inter-subject and the

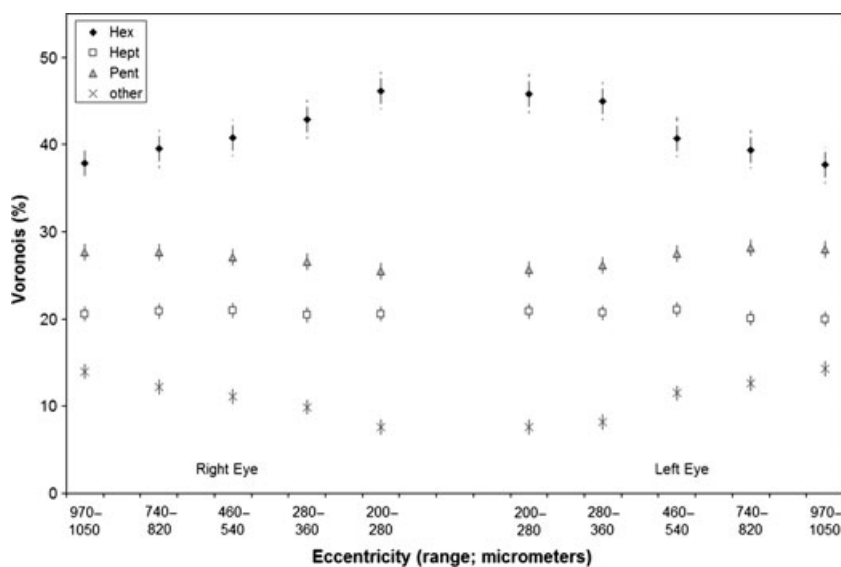


**Figure 3.** Average percentages ( $\pm$  S.D.) of Voronoi regions plotted over eccentricity in the right and left eye of the population study. The percentage of hexagonal Voronoi (black diamond) decreases at increasing eccentricity, while the percentage of pentagonal Voronoi (grey triangle) slightly increases. The percentage of Voronoi domains with  $4n$  and  $8n$  (black cross) arrangements also increases at greater eccentricities.

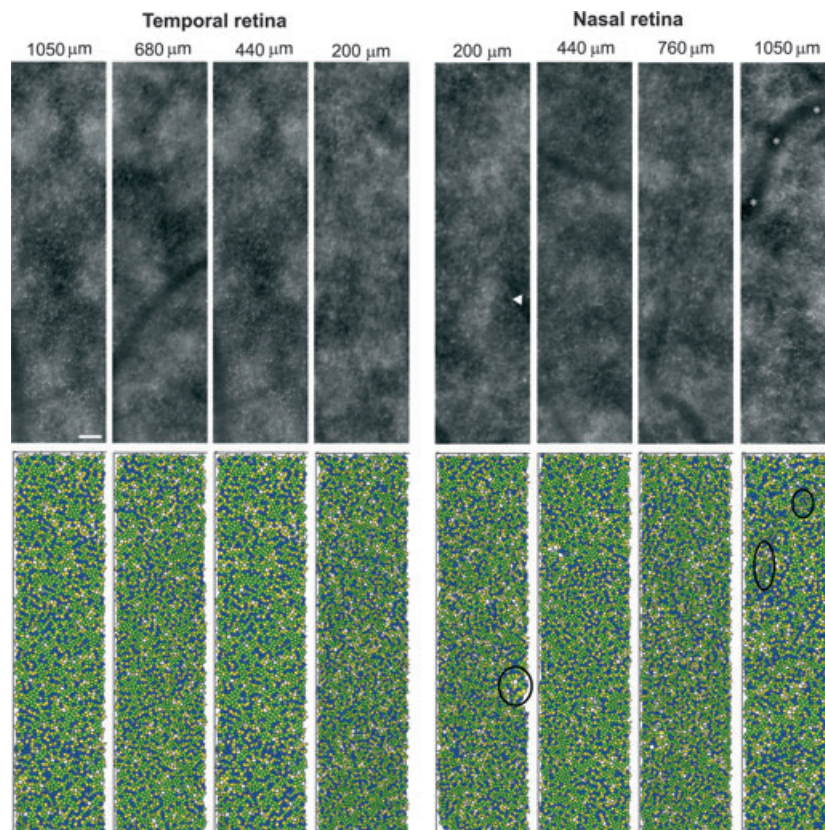


**Figure 4.** Cone mosaic and corresponding colour Voronoi diagrams of the preferred cone arrangement over parafoveal retinal sections ( $820 \times 205 \mu\text{m}$ ) at increasing eccentricity from the foveal reference point along the horizontal meridian of a 42-years old female right eye. Scale bar represents  $50 \mu\text{m}$ . A prevalence of the hexagonal pattern (green Voronoi tiles) is shown across eccentricities, though the percentage of pentagonal (yellow tiles) and heptagonal (blue tiles) Voronoi increases with increasing eccentricity. In this case, a higher percentage of heptagonal tiles and a lower percentage of hexagonal tiles occur along the nasal (5.0% and 41.9% respectively) than the temporal retina (3.2% and 47.5%) at  $1050 \mu\text{m}$  eccentricity. Variations in intensity and contrast in the image of the cone mosaic, due to large vessels (asterisks) or vessels that run vertically through the retina (triangle), rods intrusion and artefacts from image processing, may locally (black circles) reduce the accuracy of Voronoi maps to depict the preferred packing arrangements of cones.

intra-subject variation of each metric, (3) development of models of the cone mosaic to define a template to which compare presumptive abnormal cases at different retinal locations. A second advantage would be to minimise error estimates when comparing healthy and diseased eyes. In this study, we aimed to address issues 1 and 2 above and further to understand whether current models based on the preferred hexagonal arrangement of cones could be considered suitable for clinical purpose.

In this study on healthy adults subjects, cone density declined from an average 57 000- to 17 500- cones/ $\text{mm}^2$  from 250- to 1100- $\mu\text{m}$  eccentricity. The inter-subject variation of cone density ranged between 10% and 15% across eccentricities and the intra-subject variation was lower than 8% at all eccentricity locations in 17 of 19 subjects. The average cone spacing increased from 4.50- to 8.20- $\mu\text{m}$ , with an inter-subject variation of 5–7% from 250- to 1100- $\mu\text{m}$  eccentricity. Intra-subject variation of ICD was lower than

4% in all subjects, except for two cases. Overall, the inter-subject variation of both cone density and spacing values was slightly higher at 1100  $\mu\text{m}$  eccentricity. This was probably related to the variable number of rods intruding between the cones at greater eccentricities. The two subjects showing the lowest intra-subject CoV of density and spacing estimates were older than 40 years old. In our population only three subjects were older than 40 and images of the cone mosaic showed intensity and contrast comparable to those obtained in younger cases. Other factors, likely ageing,<sup>10</sup> could have contributed to influence the intra-subject variation of density and spacing in these subjects.

Along the horizontal meridian, the cone density and ICD values showed a high agreement between the nasal and temporal retinal locations of the same eye and, with a less extent, between the same and corresponding retinal locations of fellow eyes. The understanding of the distribution of cone density and spacing as a function of retinal

eccentricity in the same eye and between fellow eyes of the same subject could be of great clinical utility when monitoring a subject longitudinally over time or when comparing controls with presumptive pathologic cases.

Our results are in agreement with previous studies.<sup>10–13,36–39</sup> In general, authors showed an average decline from ~59000 cones/mm<sup>2</sup> at 0.27 mm to ~45000 cones/mm<sup>2</sup> at 0.30-mm, ~35000 cones/mm<sup>2</sup> at 0.5 mm, ~20000 cones/mm<sup>2</sup> at 1.0 mm and ~12000 cones/mm<sup>2</sup> at 1.5 mm eccentricity from the fovea.<sup>10–12</sup> In an histology study, Curcio *et al.*<sup>36</sup> showed an average increase of cone spacing from 3.30  $\mu$ m at 150  $\mu$ m eccentricity to 4.50  $\mu$ m at 400  $\mu$ m from the foveal centre. Using an AO-SLO, Merino *et al.*<sup>37</sup> showed values of cone spacing across retinal eccentricities (from an average 4- to 8- $\mu$ m between 1 and 4 degree) highly comparable with those of the present study. Duncan *et al.*<sup>38</sup> showed an average increase of cone spacing from 0.75 arc min at 0.5 degree eccentricity to 1.8 arc min at 3 degree eccentricity in eight healthy eyes. Hirsch and Miller<sup>21</sup> showed, in primate eyes, an average increase of cone spacing (measured as distance between nearest-neighbour cones) from 2.7  $\mu$ m at 0.1 degree eccentricity to 8.0  $\mu$ m at 5.6 degree eccentricity. The slight discrepancies in the estimates of cone density and spacing between the AO studies could depend on various factors, such as the inclusion of subjects with different ages and/or eyes with different axial lengths and refractive corrections, the location of the foveal reference point,<sup>4,13,39</sup> the model eye used to estimate the retinal image size, the sampling window size and the approach used to calculate cone spacing.<sup>21,39</sup> Currently, different model eyes<sup>31,40</sup> have been used to compute the corrected retinal magnification factor (RMF<sub>corr</sub>), including the method developed by Bennett *et al.*<sup>41</sup>, the Gullstrand model eye<sup>11,13,39</sup> and the Indiana model eye.<sup>10</sup> No direct evidence shows which model eye would be the most accurate one.<sup>39</sup> Another consideration when scaling the estimated cone densities is that the axial length of the eye is not identical across the retina. In our study, cone densities have been estimated between 250- and 1100- $\mu$ m eccentricities: we used a single RMF<sub>corr</sub> value to correct for the retinal image size of the AO images of the parafoveal cone mosaic, since the axial length measured at 0.6 degree is on average less than 0.4% different from the axial length measured at 6 degrees, as previously shown.<sup>31</sup> The variation of cone density and spacing values was taken relative to fixation which was assumed to be our foveal centre reference point; however, no measurement of the steady fixation was done to confirm this assumption since we were not able to resolve the smallest cones at the foveola in most subjects. Previous authors<sup>11,42</sup> found that the centre of fixation deviates on average  $18 \pm 11$   $\mu$ m from the foveal centre. In previous work, we provided an estimation of the potential error arising from taking the centre of fixation instead of

the foveal centre as reference point for distance calculation.<sup>39</sup> By laterally displacing the centre of a 50  $\times$  50  $\mu$ m sampling window by 18  $\mu$ m along the horizontal meridian, the potential error in our eccentricity-dependent cone density measurements has been estimated to be <1000 cones/mm<sup>2</sup> and <500 cones/mm<sup>2</sup> at 250- and 1300- $\mu$ m eccentricity respectively. The potential error was lower than the measurement error of the automated cone counting method.

Cone spacing showed a lower inter-subject and intra-subject variation than cone density. In this study, ICD was calculated from cone density under the assumption of a perfect hexagonal lattice. It then became less sensitive to errors in cone labelling than cone density. Such insensitivity could however be interpreted as either an advantage or a disadvantage, as previously discussed.<sup>17</sup> Though cone spacing has been claimed to be a more robust and conservative measurement than cone density for comparison among eyes,<sup>38</sup> if taken separately from each other, cone density and ICD can underestimate and overestimate the global health of the cone mosaic, respectively.

Various methods<sup>8,11–13,21,22,28,31,43–47</sup> have been used for cone spacing estimation, which included the density-count method, the fast Fourier transform (FFT)-based method and the distribution-of-distances method. The density count method, as used in this study, is derived from the number of cones per unit area: it provides a single-point estimate without a measure of variation and further depends upon the mode of packing and assumes an ordered lattice. When ICD is calculated from identified cone centre making an assumption about the preferred hexagonal cone arrangement within the sampling area, care should be taken to avoid regions of missing data (e.g. large blood vessels, image border etc.) or defects in the image.<sup>13,17</sup> The FFT-based method is not derived by cone density but it also assumes an ordered lattice.<sup>12,13</sup> The last method is assumption free and provides estimates of both central tendency and variation; there is still no work showing the reliability of this latter method in human subjects.

In our study, Voronoi analysis was performed in 1024  $\times$  128 pixels (820  $\times$  102  $\mu$ m) image sections in order to analyse the eccentricity dependent change of cone packing arrangement. We chose to represent the preferred cone packing arrangement within narrow image sections to minimise the potential negative effect of large vessels on Voronoi tessellation locally. We found that, in the parafoveal region, the human cone photoreceptors were mostly arranged hexagonally (40–50%) with the degree of regularity decreasing as the retinal eccentricity increases: the percentage of hexagonal cone arrangement diminishes, while the percentage of 4n, 5n and 8n patterns increases. Non-hexagonal Voronoi contributed less than 43% of the mosaic region up to 280  $\mu$ m eccentricity from the fovea,

but this percentage increased to more than 60% at greater eccentricities. A low variance of the preferred cone arrangement in the population was found and the cone locations showed comparable arrangements between equivalent eccentricities of the nasal and temporal regions of the same eye and between fellow eyes. These results agree with previous data reported by Dees *et al.*<sup>48</sup> using an AOSLO where the authors analysed the cone mosaic regularity between 1° and 3° eccentricity in a population of ten young adults (20–30 years) showing that 34–64% of the cones were hexagonally packed. However, the standard variation from the mean percentage of cones with 6*n* arrangement was higher than that found in the present study. Technical factors can potentially generate differences between the Voronoi maps created using images of the photoreceptor mosaic acquired via AO flood-illumination and AOSLO instruments. These factors can include variations in brightness and contrast of the cone mosaic,<sup>14–16</sup> different resolution of rods, *masking effect* by large retinal vessels, the image processing method used to produce the final image of the cone mosaic and the filtering algorithms used to identify cones.

Previous studies<sup>8,22,28,49</sup> of the foveal and parafoveal cone mosaic topography showed the prevalence of hexagonal order but also demonstrated a considerable proportion of non-hexagonal elements. Cones with 5*n* or 7*n* characterisation occurred in similar proportions across eccentricities: each from 10–20% in the rod-free area to 20–30% at increasing eccentricities. Pum *et al.*<sup>28</sup> showed the dominance (70–80%) of a crystalline hexagonal topography within the normal foveal mosaic; Li and Roorda<sup>8</sup> showed that the percentage of hexagonal Voronoi tended to decrease between 0.25 and 5 degrees from the fovea; a study on a post-mortem human retina showed that the cones were more hexagonally arranged near the edge of the fovea (between 0.20 and 0.25 degrees eccentricity) than in the foveal center.<sup>22,27</sup>

According to the current study and previous work from others,<sup>49–53</sup> a model of the parafoveal mosaic by a lattice with continuous hexagonal regularity cannot be considered completely adequate to describe the cone mosaic arrangement in a healthy eye. Though Voronoi analysis of the parafoveal mosaic confirmed the prevalence of a crystalline hexagonal topography within the normal retinas, without definition of consistent rules it is difficult to classify a ‘normative pattern’. Age-related or pathologic receptor death may deteriorate lattice quality.<sup>19,28,54–56</sup> A study<sup>28</sup> on an enucleated eye with previous diagnosis of advanced glaucoma showed a high proportion of non-hexagonal cone positions in the fovea (40% vs 20%, as said above) and a lower cone peak density as compared to healthy eyes. It is probably that receptor losses allow a repositioning of neighbouring cones. This phenomenon could also result in a higher variance of cone spacing and make the calculation

of ICD with assumption of ordered lattice not adequate for clinical purpose.

The photoreceptor mosaic is characterized by a poorly understood process of ‘self-organisation’ resulting in a lattice with various, non-random, deviations from a continuous crystalline pattern.<sup>21,22,26,28,56–58</sup> In an AO retinal image of the photoreceptor mosaic, deviations from hexagonal order can be attributed to some phenomena, such as *point defects* and *linear cracks*. ‘Point defects’ of the cone lattice occur within otherwise intact mosaic areas and may be likely represented by smaller cones (S cones), cones with no wave guiding properties or isolated rods (it is plausible that rods cannot be always distinguished by point defects) and vessels that run vertically through the retinal layers. ‘Linear cracks’ appear as irregular lines of cones of variable extension demarcating polygonal subdivisions of the hexagonal lattice areas<sup>27</sup>: most non-hexagonal cone positions are not dispersed diffusely but appear arranged in linear series. This results in cracks demarcating polygonal subdivisions of the hexagonal lattice areas. In the parafovea, the 5*n* and 7*n* locations tended to be aligned in curved lines surrounding patches of hexagonal mosaic of variable extension (Figure 5). Previous authors<sup>3,22,27</sup> have also shown that the mosaic does not form a single crystalline array but a variable number of ordered hexagonal domains: the domains differed in orientation and were separated by irregular lines of cones (i.e. the linear cracks) with 4*n*, 5*n*, 7*n* or 8*n* characterisation. In general, cones appear not to be randomly aligned, but tightly clustered with the preferred arrangement that varies as a function of retinal eccentricity. The type and quality of the cone lattice is supposed to be of high importance for the inter-receptor network and cell signalling.<sup>28</sup> Other phenomena that can contribute to change the hexagonal order are represented by local variance of the cone shape and the compression along the vertical meridian as a consequence of the expansion along the horizontal meridian of the photoreceptor mosaic.<sup>12,22,24,27,28,53</sup> Further work is needed to understand the biological, functional and mechanical factors involved in the parafoveal cone mosaic organization.<sup>59</sup>

When reporting normative data, it is currently recommended to show the repeatability statistics of the method used to identify cones. This approach could be helpful to quantify and compare the measurement error for each of the automated method used. Our results were in agreement with those previously shown.<sup>17,18,39</sup> The error in cone density estimates can be attributed to cone selection, magnification error, distortion in cone images, selection of the region of interest and sampling area, misleading identification of rods as cones.

The knowledge of cone spacing and packing arrangement could be useful to understand the normal range of cone positions and to monitor pathological changes of the cone

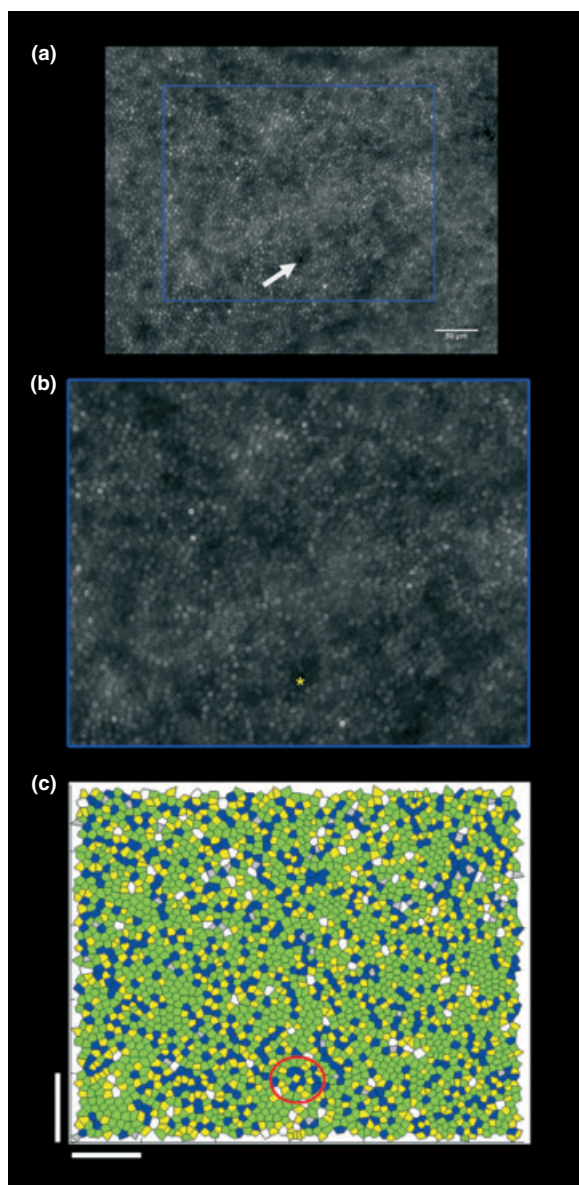


**Figure 5.** (a) Adaptive optics image of the parafoveal photoreceptor mosaic centred at  $2.5^\circ$  temporally from the foveal centre (scale bar  $50\ \mu\text{m}$ ). The white arrow indicates a 'point defect' in the image. Such point defects of the cone lattice occur within otherwise intact mosaic areas. These defects may be due to cones with rod-like appearance, cones with no wave guiding properties, rods, to a blood vessel running vertically through the entire retina. The blue window encloses the cone mosaic area for subsequent Voronoi analysis. (b) The point defect (yellow asterisk) is not labelled by the automated procedure. (c) Voronoi tiles showing that point defects can induce an irregular pattern distribution of cones (red circle): the nearest neighbours in the image section are not the nearest neighbours in the real population of photoreceptors (*undersampling effect*). In a Voronoi tiles, the cone mosaic consists of a lattice with various, probably non-random, deviations from a continuous hexagonal pattern: Voronoi with  $7n$  and  $5n$  arrangements (blue and yellows tiles) usually are lined up surrounding clusters of hexagonal Voronoi (green tiles). Scale bars represent  $50\ \mu\text{m}$ .

mosaic over time when cone density falls within the normal range. The exploitation of AO retinal imaging to follow up changes of cone spacing and packing, other than cone density, longitudinally over time could be of great clinical utility; deviations in the expected cone organisation could be described with more sensitivity using complementary methods.

### Acknowledgments

The authors are thankful to Kacie Li for generously providing the up-to-date source code for the routine used to label the cone photoreceptors and for his valuable comments to the manuscript. The writing of this manuscript was supported in part by the National Framework Program for Research and Innovation (grant PON\_01\_00110).

### Disclosure

The authors report no conflicts of interest and have no proprietary interest in any of the materials mentioned in this article.

### References

- Godara P, Dubis AM, Roorda A, Duncan JL & Carroll J. Adaptive Optics retinal imaging: emerging clinical applications. *Optom Vis Sci* 2010; 87: 930–941.
- Roorda A. Adaptive optics for studying visual function: a comprehensive review. *J Vision* 2011; 11: 1–21.
- Dubra A, Sulai Y, Norris JL *et al.* Noninvasive imaging of the human rod photoreceptor mosaic using a confocal adaptive optics scanning ophthalmoscope. *Biomed Opt Express* 2011; 2: 1864–1876.
- Lombardo M, Serrao S, Ducoli P & Lombardo G. Adaptive optics photoreceptor imaging. *Ophthalmology* 2012; 119: 1498–198e2.
- Tam J, Martin JA & Roorda A. Noninvasive visualization and analysis of parafoveal capillaries in humans. *Invest Ophthalmol Vis Sci* 2010; 51: 1691–1698.
- Takayama K, Ooto S, Hangai M *et al.* High-resolution imaging of the retinal nerve fiber layer in normal eyes using adaptive optics scanning laser ophthalmoscopy. *PLoS ONE* 2012; 7: e33158.
- Huang G, Qi X, Chui TY, Zhong Z & Burns SA. A clinical planning module for adaptive optics SLO imaging. *Optom Vis Sci* 2012; 89: 593–601.
- Li KY & Roorda A. Automated identification of cone photoreceptors in adaptive optics retinal images. *J Opt Soc Am A* 2007; 24: 1358–1363.
- Xue B, Choi SS, Doble N & Werner JS. Photoreceptor counting and montaging of en-face retinal images from an adaptive optics fundus camera. *J Opt Soc Am A* 2007; 24: 1364–1372.

10. Song H, Chui TYP, Zhong Z, Elsner AE & Burns SA. Variation of cone photoreceptor packing density with retinal eccentricity and age. *Invest Ophthalmol Vis Sci* 2011; 52: 7376–7384.
11. Li KY, Tiruveedhula P & Roorda A. Intersubject variability of foveal cone photoreceptor density in relation to eye length. *Invest Ophthalmol Vis Sci* 2010; 51: 6858–6867.
12. Chui TYP, Song H & Burns S. Adaptive-optics imaging of human cone photoreceptor distribution. *J Opt Soc Am A* 2008; 25: 3021–3029.
13. Lombardo M, Serrao S, Ducoli P & Lombardo G. Variations in the image optical quality of the eye and the sampling limit of resolution of the cone mosaic with axial length in young adults. *J Cataract Refract Surg* 2012; 38: 1147–1155.
14. Rha J, Schroeder B, Godara P & Carroll J. Variable optical activation of human cone photoreceptors visualized using a short coherence light source. *Opt Lett* 2009; 34: 3782–3784.
15. Pircher M, Kroisamer JS, Felberer F, Sattmann H, Götzinger E & Hitzenberger CK. Temporal changes of human cone photoreceptors observed *in vivo* with SLO/OCT. *Biomed Opt Express* 2010; 2: 100–112.
16. Rha J, Jonnal RS, Thorn KE, Qu J, Zhang Y & Miller DT. Adaptive optics flood-illumination camera for high-speed retinal imaging. *Opt Express* 2006; 14: 4552–4569.
17. Garrioch R, Langlo C, Dubis AM, Cooper RF, Dubra A & Carroll J. Repeatability on *in vivo* cone density and spacing measurements. *Optom Vis Sci* 2012; 89: 632–643.
18. Talcott KE, Ratman K, Sundquist SM *et al.* Longitudinal study of cone photoreceptors during retinal degeneration and in response to ciliary neurotrophic factor treatment. *Invest Ophthalmol Vis Sci* 2011; 52: 2219–2226.
19. Godara P, Siebe C, Rha J, Michaelides M & Carroll J. Assessing the photoreceptor mosaic over drusen using adaptive optics and SD-OCT. *Ophthalmic Surg Lasers Imaging* 2010; 41(Suppl): S104–S108.
20. Godara P, Wagner-Schuman M, Rha J, Connor TB Jr, Stepien KE & Carroll J. Imaging the photoreceptor mosaic with adaptive optics: beyond counting cones. *Adv Exp Med Biol* 2012; 723: 451–458.
21. Hirsch J & Miller WH. Does cone positional disorder limit resolution? *J Opt Soc Am A* 1987; 4: 1481–1492.
22. Curcio CA & Sloan KR. Packing geometry of human cone photoreceptors: variation with eccentricity and evidence of local anisotropy. *Vis Neurosci* 1992; 9: 169–180.
23. Marcos S, Tornow RP, Elsner AE & Navarro R. Foveal cone spacing and cone photopigment density differences: objective measurements in the same subjects. *Vision Res* 1997; 37: 1909–1915.
24. Williams DR. Topography of the foveal cone mosaic in the living human eye. *Vision Res* 1988; 28: 433–454.
25. Williams DR & Coletta NJ. Cone spacing and the visual resolution limit. *J Opt Soc Am A* 1987; 4: 1514–1523.
26. Yellott JE Jr. Spectral analysis of spatial sampling by photoreceptors: topological disorder prevents aliasing. *Vision Res* 1982; 22: 1205–1210.
27. Wojtas DH, Wu B, Ahnelt PK, Bones PJ & Millane RP. Automated analysis of differential interference contrast microscopy images of the foveal cone mosaic. *J Opt Soc Am A* 2008; 25: 1181–1189.
28. Pum D, Ahnelt PK & Grasl M. Iso-orientation areas in the foveal cone mosaic. *Vis Neurosci* 1990; 5: 511–523.
29. Rodieck RW. The density recovery profile: a method for the analysis of points in the plane applicable to retinal studies. *Vis Neurosci* 1991; 6: 95–111.
30. Brostow W, Dussault J-P & Fox BL. Construction of Voronoi polyhedra. *J Comput Phys* 1978; 29: 81–92.
31. Drasdo N & Fowler CW. Non-linear projection of the retinal image in a wide-angle schematic eye. *Br J Ophthalmol* 1974; 58: 709–714.
32. Coletta NJ & Watson T. Effect of myopia on visual acuity measured with laser interference fringes. *Vision Res* 2006; 46: 636–651.
33. Chui TYP, Song H & Burns S. Individual variations in human cone photoreceptor packing density: variations with refractive error. *Invest Ophthalmol Vis Sci* 2008; 49: 4679–4687.
34. Bland JM & Altman DG. Measurement error proportional to the mean. *BMJ* 1996; 313: 106.
35. Bland JM & Altman DG. Measurement error and correlation coefficients. *BMJ* 1996; 313: 41.
36. Curcio CA, Sloan KR, Kalina RE & Hendrickson AE. Human photoreceptor topography. *J Comp Neurol* 1990; 292: 497–523.
37. Merino D, Duncan JL, Tiruveedhula P & Roorda A. Observation of cone and rod photoreceptors in normal subjects and patients using a new generation adaptive optics scanning laser ophthalmoscope. *Biomed Opt Express* 2011; 2: 2189–2201.
38. Duncan JL, Zhang Y, Gandhi J *et al.* High-resolution imaging with adaptive optics in patients with inherited retinal degeneration. *Invest Ophthalmol Vis Sci* 2007; 48: 3283–3291.
39. Lombardo M, Lombardo G, Schiano Lomoriello D, Ducoli P, Stirpe M & Serrao S. Interocular symmetry of parafoveal photoreceptor cone density distribution. *Retina* 2013; in press.
40. de Almeida MS & Carvalho LA. Different schematic eyes and their accuracy to the *in vivo* eye: a quantitative comparison study. *Braz J Phys* 2007; 37: 378–387.
41. Bennett AG, Rudnicka AR & Edgar DF. Improvements on Littmann's method of determining the size of retinal features by fundus photography. *Graefes Arch Clin Exp Ophthalmol* 1994; 232: 361–367.
42. Putnam NM, Hofer HJ, Doble N, Chen L, Carroll J & Williams DR. The locus of fixation and the foveal cone mosaic. *J Vis* 2005; 5: 632–639.

43. Hirsch J & Hylton R. Quality of the primate photoreceptor lattice and limits of spatial vision. *Vision Res* 1984; 24: 347–356.
44. Dowling JE. Foveal receptors of the monkey retina: fine structure. *Science* 1965; 147: 57–59.
45. Krebs W & Krebs IP. Quantitative morphology of the central fovea in the primate retina. *Am J Anat* 1989; 184: 225–236.
46. Borwein B, Borwein D, Medeiros J & McGowan JW. The ultrastructure of monkey foveal photoreceptors, with special reference to the structure, shape, size, and spacing of the foveal cones. *Am J Anat* 1980; 159: 125–146.
47. Ahnelt PK, Kolb H & Pflug R. Identification of a subtype of cone photoreceptor, likely to be blue sensitive, in the human retina. *J Comp Neurol* 1987; 255: 18–34.
48. Dees EW, Dubra A & Baraas RC. Variability in parafoveal cone mosaic in normal trichromatic individuals. *Biomed Opt Express* 2011; 2: 1351–1358.
49. da Fontoura Costa L, Oliveira Bonci DM, Saito CA, de Farias Rocha FA, de Lima Silveira LC & Ventura DF. Voronoi analysis uncovers relationship between mosaics of normally placed and displaced amacrine cells in the thraira retina. *Neuroinformatics* 2005; 5: 59–77.
50. da Fontoura Costa L. Characterizing polygonality in biological structures. *Phys Rev E Stat Nonlin Soft Matter Phys* 2006; 73: 011913.
51. Shapiro MB, Schein SJ & de Monasterio FM. Regularity and Structure of the Spatial Pattern of Blue Cones of Macaque Retina. *J Am Stat Assoc* 1985; 80: 803–812.
52. Duyckaerts C & Godefroy G. Voronoi tessellation to study the numerical density and the spatial distribution of neurones. *J Chem Neuroanat* 2000; 20: 83–92.
53. Hendrickson AE & Youdelis C. The morphological development of the human fovea. *Ophthalmology* 1984; 91: 603–612.
54. Ooto S, Hangai M, Takayama K *et al.* High-resolution imaging of the photoreceptor layer in epiretinal membrane using adaptive optics scanning laser ophthalmoscopy. *Ophthalmology* 2011; 118: 873–881.
55. Boretsky A, Khan F, Burnett G *et al.* *In vivo* imaging of photoreceptor disruption associated with age-related macular degeneration: a pilot study. *Lasers Surg Med* 2012; 44: 603–610.
56. Kram YA, Mantey S & Corbo JC. Avian cone photoreceptors tile the retina as five independent, self-organizing mosaics. *PLoS ONE* 2010; 5: 1–12.
57. Cook JE. Spatial properties of retinal mosaics: an empirical evaluation of some existing measures. *Vis Neurosci* 1996; 13: 15–30.
58. Williams DR. Aliasing in human foveal vision. *Vision Res* 1985; 25: 195–202.
59. Burns SA, Wu S, He JC & Elsner AE. Variations in photoreceptor directionality across the central retina. *J Opt Soc Am A* 1997; 14: 2033–2040.

### Supporting Information

Additional Supporting Information may be found in the online version of this article:

**Table S1.** Correlation matrix of cone density values.

**Table S2.** Correlation matrix of center-to-center cone distance (ICD) values.